Mechanics of Advanced Materials and Structures

ISSN: (Print) (Online) Journal homepage: www.tandfonline.com/journals/umcm20

Artificial neural network-enhanced mathematical simulation based on Carrera unified formulation for dynamic analysis and structural integrity assessment of advanced nanocomposites reinforced tunnel structures

Xiaoming You, Gongxing Yan, Khalid A. Alnowibet & Mohammed El-Meligy

MECHANICS OF ADVANCED MATERIALS AND STRUCTURES
https://doi.org/10.1080/15376494.2024.2414947

ORIGINAL ARTICLE

Artificial neural network-enhanced mathematical simulation based on Carrera unified formulation for dynamic analysis and structural integrity assessment of advanced nanocomposites reinforced tunnel structures

Xiaoming You[a], Gongxing Yan[b,c], Khalid A. Alnowibet[d], and Mohammed El-Meligy[e,f]

[a]College of Civil Engineering, Chongqing Vocational Institute of Engineering, Chongqing, China; [b]School of Intelligent Construction, Luzhou Vocational and Technical College, Luzhou, Sichuan, China; [c]Luzhou Key Laboratory of Intelligent Construction and Low-Carbon Technology, Luzhou, China; [d]Statistics and Operations Research Department, College of Science, King Saud University, Riyadh, Kingdom of Saudi Arabia; [e]Jadara University Research Center, Jadara University, Irbid, Jordan; [f]Applied Science Research Center, Applied Science Private University, Amman, Jordan

ABSTRACT

This article presents the application of the Carrera Unified Formulation (CUF) for dynamic analysis and structural integrity assessment of advanced nanocomposite-reinforced tunnel structures. CUF offers a generalized framework that simplifies the modeling of complex structures, providing an efficient approach to address the dynamic behavior of nanocomposites. Advanced nanocomposites, which enhance mechanical performance and durability, are increasingly used in critical infrastructure such as tunnel systems. Traditional methods often fall short in capturing the intricate interactions within these materials, particularly under dynamic loads. CUF overcomes these challenges by incorporating higher-order theories and multi-scale analysis, allowing for accurate prediction of displacements, stresses, and potential failure modes. To further validate the results, an Artificial Neural Network (ANN) model is trained using simulated data, ensuring robust predictions for various loading conditions. The ANN assists in approximating the dynamic response and integrity of the structure, enabling real-time assessments with minimal computational expense. The combined CUF-ANN approach demonstrates high accuracy and efficiency, making it a reliable tool for the structural integrity assessment of nanocomposite-reinforced tunnels. This study highlights the significant potential of integrating CUF and ANN for the analysis and design of advanced engineering structures subjected to dynamic environmental conditions.

ARTICLE HISTORY
Received 21 August 2024
Accepted 7 October 2024

KEYWORDS
Carrera unified formulation; optimization; machine learning; advanced nanocomposites; linear programming

1. Introduction

Advanced composite materials have revolutionized modern engineering due to their exceptional mechanical properties and versatility [1–3]. These materials, made from two or more distinct constituents, offer superior strength-to-weight ratios compared to traditional materials like steel or aluminum [4, 5]. Engineers value composites for their ability to be tailored to specific design requirements, allowing for customized stiffness, strength, and thermal properties [6, 7]. The high durability and corrosion resistance of composites make them ideal for demanding environments, such as aerospace, automotive, and marine industries [8, 9]. Their lightweight nature also contributes to significant energy savings, particularly in transportation, where reduced weight leads to lower fuel consumption [10–12]. Additionally, composite materials can absorb more energy during impacts, providing enhanced safety in crash-prone applications [13, 14]. Engineers also benefit from the fatigue resistance of composites, allowing for longer service life in structures subjected to repetitive loading [15–17]. Their ability to integrate sensors and other smart technologies makes composites a key player in the development of smart infrastructure and advanced structural health monitoring systems [18]. In civil engineering, composites are used to reinforce aging structures, improving their load-bearing capacity without adding excessive weight [19]. Advanced composites offer significant design flexibility, enabling the creation of complex shapes that would be difficult or impossible with conventional materials [20, 21]. This leads to more efficient designs, reducing the number of components and minimizing assembly costs [22]. Engineers can also take advantage of the material's anisotropy, aligning fibers in specific directions to optimize performance under different loads [23]. In summary, advanced composites provide engineers with a toolkit for designing high-performance, efficient, and durable structures, making them crucial in industries where performance and weight are critical considerations [24, 25]. As research in nanocomposites and bio-composites progresses, their importance in future engineering solutions will continue to grow, addressing sustainability, and environmental challenges [26, 27].

The Carrera unified formulation is highly significant in the modeling of complex structures, particularly for engineers dealing with advanced materials and systems [28]. CUF provides a generalized framework that simplifies the development of mathematical models for structural analysis, especially in cases where traditional methods may fall short [29]. Its versatility

CONTACT Gongxing Yan yaaangx@126.com School of Intelligent Construction, Luzhou Vocational and Technical College, Luzhou, Sichuan, China.

allows engineers to model various types of structures, such as beams, plates, and shells, with the same formulation, regardless of the complexity or scale [30]. One of the primary advantages of CUF is its ability to handle structures made of advanced materials, such as composites, functionally graded materials, and nanocomposites [31]. These materials exhibit behaviors that are often difficult to capture using classical theories [30]. CUF simplifies this by enabling the implementation of higher-order theories, improving the accuracy of results without significantly increasing computational effort [25]. CUF is particularly valuable in multi-scale analysis, where engineers need to understand the behavior of structures at different levels, from the microstructure of materials to the macroscopic scale of entire components [32].

Modeling plays a crucial role in engineering and science as it allows professionals to represent complex real-world systems in a simplified, mathematical form [33, 34]. By creating models, engineers can simulate physical processes, predict behavior, and evaluate performance without the need for costly experiments or prototypes [35, 36]. This helps in understanding how a system will perform under various conditions, reducing uncertainties and risks before real-world implementation [37, 38]. One of the key advantages of modeling is its ability to provide insights into systems that are difficult or impossible to test directly, such as large infrastructure or extreme environmental conditions [39, 40]. It enables the optimization of designs by allowing engineers to tweak parameters and analyze different scenarios efficiently [41, 42]. This saves time and resources, making the development process more cost-effective [43, 44]. Modeling is essential in fields like fluid dynamics, structural analysis, and thermal management, where understanding how systems behave under various forces and temperatures is critical [45, 46]. For example, in aerospace, models help predict aerodynamic forces and structural integrity without needing full-scale wind tunnel testing [47, 48]. Similarly, in civil engineering, models are used to assess load-bearing capacities and the stability of buildings, bridges, and tunnels [20, 49]. Moreover, modeling can enhance safety by identifying potential failure modes and weak points in systems before they occur in real-life applications [21, 50]. Engineers also use models to simulate dynamic behaviors such as vibrations, shocks, or impacts, ensuring structures can withstand unpredictable forces [51, 52]. In addition to its predictive power, modeling facilitates communication between engineers, researchers, and stakeholders by providing a clear representation of complex systems [53, 54]. As computational tools and simulation software evolve, modeling continues to become more accessible and accurate, further boosting its importance in modern engineering [55, 56]. Overall, modeling is a critical step in the design, analysis, and decision-making process, helping engineers to build efficient, safe, and innovative solutions across various industries [57, 58]. The aim of Ref. [59] was to enhance economic stability through targeted financial strategies and risk management by employing advanced algorithms to categorize credit card users according to their financial behaviors. To effectively identify and assess tail risks in financial markets, Ref. [60] employs extreme value theory along with mixture models to estimate the likelihood of rare but substantial financial losses.

This work describes the use of the CUF for advanced nanocomposite-reinforced tunnel constructions' dynamic analysis and structural integrity evaluation. With its generalized framework, CUF makes complicated structural modeling easier and gives a productive way to deal with nanocomposites' dynamic behavior. Advanced nanocomposites are being used more often in vital infrastructure, such tunnel systems, since they improve mechanical performance and longevity. Conventional techniques often fail to capture the complex interactions that exist inside these materials, especially when subjected to dynamic stresses. By using multi-scale analysis and higher-order theories, CUF overcomes these difficulties and enables precise prediction of displacements, stresses, and probable failure modes. An ANN model is trained using simulated data to further evaluate the outcomes and guarantee reliable predictions under different loading scenarios. The artificial neural network helps to approximate the structure's integrity and dynamic reactivity, allowing for real-time evaluations at low computing cost. Because of its excellent accuracy and efficiency, the combined CUF-ANN technique is a dependable instrument for evaluating the structural integrity of tunnels reinforced with nanocomposite materials. The substantial potential of combining CUF and ANN for the analysis and design of sophisticated engineering structures exposed to changing environmental conditions is shown by this work.

2. Basic equation

Tunnel structure in schematic and zones is shown in Figure 1. As is presented the tunnel structure has two curvature parameters (R_1 and R_2) and thickness h. Also, the tunnel structure is under transient external loading as demonstrated by $F(t)$.

2.1. Graphene origami-enabled auxetic metamaterial

Figure 2 shows the different GOP reinforcement distribution.

Table 1 lists the material characteristics of the GOPs reinforcement and concrete matrix.

The Halpin-Tsai homogenization approach is extended to determine the material characteristics. The Young's modulus may now be expressed as follows:

$$E_c = 0.49 \times \frac{1+\xi_L\eta_L V_{GOP}}{1-\eta_L V_{GOP}} \times E_m + 0.51 \times \frac{1+\xi_t\eta_t V_{GOP}}{1-\eta_t V_{GOP}} \times E_m, \tag{1}$$

in which, $\xi_L = \xi_t = 2\frac{d_{GOP}}{h_{GOP}}$, $\mathrm{V}^*_{GOP} = \frac{W_{GOP}}{W_{GOP}+\left(\frac{\rho_{GPL}}{\rho_M}\right)(1-W_{GOP})}$, $\eta_l = -\frac{1-\left(\frac{E_{GOP}}{E_M}\right)}{\xi_l+\left(\frac{E_{GOP}}{E_m}\right)}$, and $\eta_t = -\frac{1-\left(\frac{E_{GOP}}{E_M}\right)}{\xi_t+\left(\frac{E_{GOP}}{E_m}\right)}$. The effective Poisson's ratio, and density may be obtained by using the mixing rule from

$$\nu_c = \nu_{GOP} V_{GOP} + \nu_m(1-V_{GOP}), \tag{2a}$$

$$\rho_c = \rho_{GOP} V_{GOP} + \rho_m(1-V_{GOP}). \tag{2b}$$

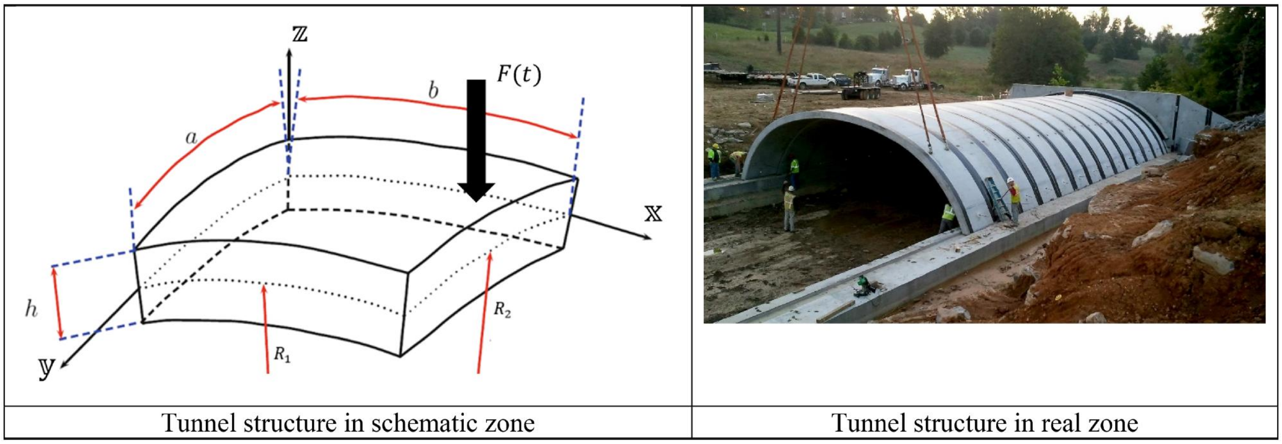

Figure 1. Tunnel structure in schematic and zones.

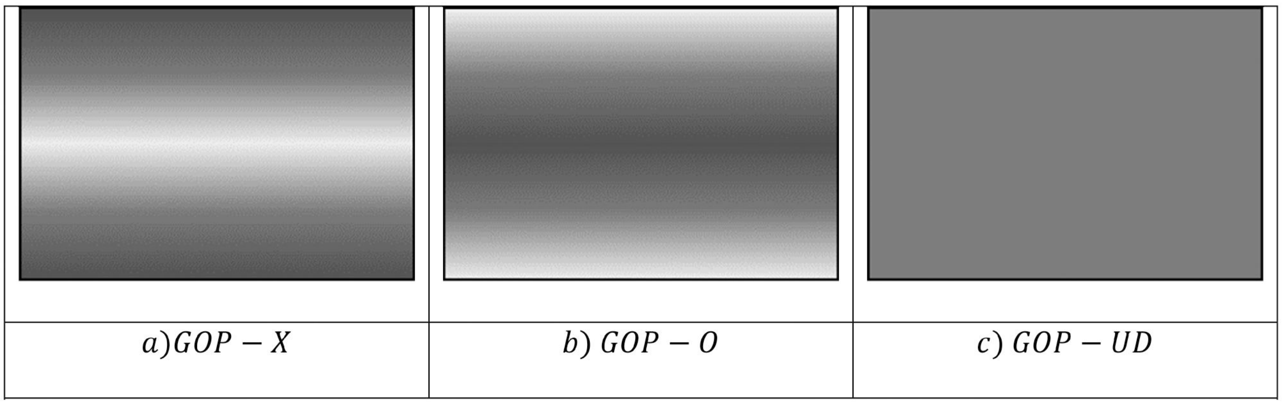

Figure 2. The various distribution of GOP reinforcement

Table 1. Material properties of the system.

Concrete (matrix)	GOPs
$\nu_m = 0.2$	$\nu_{GOP} = 0.165$
$\rho_m \left(\frac{\mathrm{kg}}{\mathrm{m}^3}\right) = 2300$	$\rho_{GOP} \left(\frac{\mathrm{kg}}{\mathrm{m}^3}\right) = 1090$
E_m (GPa) $= 25$	E_{GOP} (GPa) $= 444.8$
	$d_{GOP}(\mathrm{nm}) = 500$
	$t_{GOP}(\mathrm{nm}) = 0.95$

Furthermore, effective shear modulus is required.

$$G_c = \frac{E_c}{2(1+\nu_c)}, \tag{3}$$

Lastly, the following GOP distribution types may be provided together with the direction of thickness:

$$X - GOP : V_{GOP}(k) = 4V^*_{GOP}|\frac{\mathbb{z}_k}{h}|, \tag{4a}$$

$$O - GOP : V_{GOP}(k) = 2V^*_{GOP}\left(1 - 2\left|\frac{\mathbb{z}_k}{h}\right|\right), \tag{4b}$$

$$UD - GOP : V_{GOP}(k) = V^*_{GOP}. \tag{4c}$$

Here, $\mathbb{z}_k = -\frac{h}{2} + \frac{(k-1)\times h}{N_L - 1}$, and $k = 1, 2, 3, \ldots, N_L$.

2.2. Carrera unified formulation and finite elements

The Carrera unified formulation was used to derive the structural theories examined in this study. The specification of the reference system serves as the introduction to the selected modeling technique based on the CUF. Figure 1 shows the one used for 2D multi-layered shell models. The reference frame is curved, with z running down the thickness and $\mathbb{x}$ and $\mathbb{y}$ matching the primary curvature lines. We took into consideration doubly curved shells with curvature radii of R_1 and R_2. The mid-surface of the kth layer is denoted by Ω_k, and its thickness is indicated by h_k. The displacement field's expansion functions are used to construct the models under analysis. By incorporating so-called expansion functions F_τ, it is feasible to construct improved 2D models inside the framework of the CUF that provide an advanced description of the through-the-thickness mechanical behavior. Next, the displacement field may be written as follows:

$$\mathbb{u}(\alpha, \beta, z) = (\mathcal{U}, \mathcal{V}, \mathcal{W}) = F_\tau(z)\mathbb{u}_\tau(\mathbb{x}, \mathbb{y}), \tau = 0, \ldots, \mathcal{N} \tag{5}$$

where $\mathbb{u}_\tau$ is the set of generalized displacement unknowns and $\mathcal{N}$ is the number of terms in the expansion. In the same way, the Einstein notation is used to τ and to the rest of this section. As a point of reference, the following fourth-order Taylor polynomial expansion is applied to all three displacement components:

$$\mathcal{U} = u_{x_1} + z u_{x_2} + z^2 u_{x_3} + z^3 u_{x_4} + z^4 u_{x_5}, \tag{6a}$$

$$\mathcal{V} = u_{y_1} + z u_{y_2} + z^2 u_{y_3} + z^3 u_{y_4} + z^4 u_{y_5}, \tag{6b}$$

$$\mathcal{W} = u_{z_1} + z u_{z_2} + z^2 u_{z_3} + z^3 u_{z_4} + z^4 u_{z_5}. \tag{6c}$$

The kth layer is taken into consideration in the FE formulation of the displacement field, which interpolates on the element nodes using the shape functions $\mathcal{N}_i$

$$u^k(x,y,z) = F_\tau^k(z)\mathcal{N}_i(x,y)u_{\tau i}^k, \tau = 0,\dots,\mathcal{N} \ \ i = 1,\dots,\mathcal{N}_n \tag{7}$$

where $u_{\tau i}^k$ denotes the nodal generalized displacement variables and $\mathcal{N}_n$ is the number of nodes in the element. The displacement field variation may be expressed as follows:

$$\delta u^k(x,y,z) = F_s^k(z)\mathcal{N}_j(x,y)\delta u_{sj}^k . s = 0,\dots,\mathcal{N} \ \ j = 1,\dots,\mathcal{N}_n \tag{8}$$

The following geometric relations may be used to derive the strain components that are in-plane (ϵ_p^k) and out-of-plane (ϵ_n^k):

$$\mathcal{E}_p^k = \left\{ \mathcal{E}_{xx}^k, \mathcal{E}_{yy}^k, \mathcal{E}_{xy}^k \right\}^T = (\mathcal{D}_p^k + \mathcal{A}_p^k)u^k, \tag{9a}$$

$$\mathcal{E}_n^k = \left\{ \mathcal{E}_{xz}^k, \mathcal{E}_{yz}^k, \mathcal{E}_{zz}^k \right\}^T = (\mathcal{D}_{n\Omega}^k + \mathcal{D}_{nz}^k - \mathcal{A}_n^k)u^k. \tag{9b}$$

The matrices $\mathcal{D}_p^k$, $\mathcal{D}_{n\Omega}^k$, $\mathcal{D}_{nz}^k$, $\mathcal{A}_p^k$, and $\mathcal{A}_n^k$ are:

$$\mathcal{D}_p^k = \begin{bmatrix} \frac{\partial_x}{\mathcal{H}_x^k} & 0 & 0 \\ 0 & \frac{\partial_y}{\mathcal{H}_y^k} & 0 \\ \frac{\partial_y}{\mathcal{H}_y^k} & \frac{\partial_x}{\mathcal{H}_x^k} & 0 \end{bmatrix}, \mathcal{D}_{n\Omega}^k = \begin{bmatrix} 0 & 0 & \frac{\partial_x}{\mathcal{H}_x^k} \\ 0 & 0 & \frac{\partial_y}{\mathcal{H}_y^k} \\ 0 & 0 & 0 \end{bmatrix}, \mathcal{D}_{nz}^k = \begin{bmatrix} \partial_z & 0 & 0 \\ 0 & \partial_z & 0 \\ 0 & 0 & \partial_z \end{bmatrix}, \tag{10a}$$

$$\mathcal{A}_p^k = \begin{bmatrix} 0 & 0 & \frac{1}{\mathcal{H}_x^k R_1^k} \\ 0 & 0 & \frac{1}{\mathcal{H}_y^k R_2^k} \\ 0 & 0 & 0 \end{bmatrix}, \mathcal{A}_n^k = \begin{bmatrix} \frac{1}{\mathcal{H}_x^k R_1^k} & 0 & 0 \\ 0 & \frac{1}{\mathcal{H}_y^k R_2^k} & 0 \\ 0 & 0 & 0 \end{bmatrix}. \tag{10b}$$

$\mathcal{H}_x^k$, and $\mathcal{H}_y^k$ are defined as:

$$\mathcal{H}_x^k = A^k(1 + z_k/R_1^k), \tag{11a}$$

$$\mathcal{H}_y^k = B^k(1 + z_k/R_2^k). \tag{11b}$$

The thickness coordinate across the kth layer is denoted by z_k, and the coefficients of the first basic form of $\boldsymbol{\Omega}_k$ are A^k, and B^k. $A^k = B^k = 1$ for shells with constant curvature radii. These geometrical characteristics are described in greater detail in Ref. [61].

This work employed shell finite elements with nine nodes, which were produced by interpolating the displacements using Lagrange shape functions. As seen in Figure 3, shape functions are defined on a local reference system of

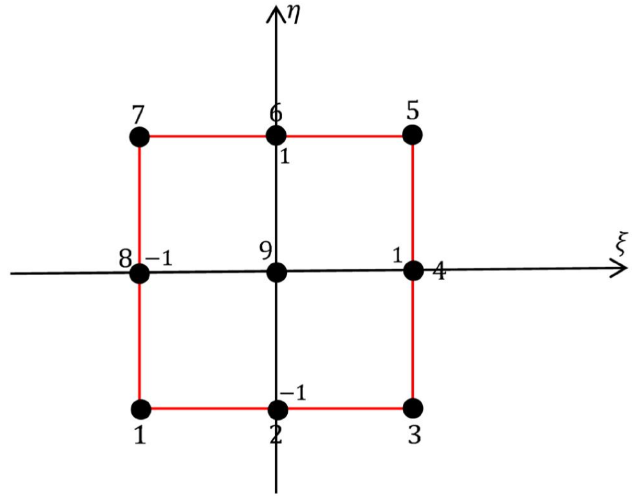

Figure 3. Nine-node finite element, Q9.

the nine-node element $-1 \le \xi, \eta \le 1$; their precise form is available in Ref. [62]. As per the FE formulation, the geometric relations take on the following form:

$$\mathcal{E}_p^k = F_\tau(\mathcal{D}_p^k + \mathcal{A}_p^k)(\mathcal{N}_i\mathbf{I})u_{\tau i}^k, \tag{12a}$$

$$\mathcal{E}_n^k = F_\tau(\mathcal{D}_{n\Omega}^k - \mathcal{A}_n^k)(\mathcal{N}_i\mathbf{I})u_{\tau i}^k + F_{\tau,z}(\mathcal{N}_i\mathbf{I})u_{\tau i}^k. \tag{12b}$$

where the identity matrix is me. The Mixed Interpolation of Tensorial Components (MITC) method was used in this study [63, 64].

This formulation states that certain interpolation techniques are used to determine the strain components. First, the element local coordinate system defines three sets of interpolation points, sometimes called "tying points." As stated clearly in Figure 4, each set of points is used for the interpolation of distinct strain components using the corresponding interpolation algorithms. The following is a useful grouping of the interpolation functions:

$$\mathbf{N}_{m1} = [\mathcal{N}_{A1}, \mathcal{N}_{B1}, \mathcal{N}_{C1}, \mathcal{N}_{D1}, \mathcal{N}_{E1}, \mathcal{N}_{F1}], \tag{13a}$$

$$\mathbf{N}_{m2} = [\mathcal{N}_{A2}, \mathcal{N}_{B2}, \mathcal{N}_{C2}, \mathcal{N}_{D2}, \mathcal{N}_{E2}, \mathcal{N}_{F2}], \tag{13b}$$

$$\mathbf{N}_{m3} = [\mathcal{N}_P, \mathcal{N}_Q, \mathcal{N}_R, \mathcal{N}_S]. \tag{13c}$$

The reader may consult [62] for further information about the mathematical formulation of MITC. The following is the interpolation of the strain components:

$$\mathcal{E}_p^k = \begin{bmatrix} \mathbf{N}_{m_1} & 0 & 0 \\ 0 & \mathbf{N}_{m_2} & 0 \\ 0 & 0 & \mathbf{N}_{m_3} \end{bmatrix} \begin{bmatrix} \mathcal{E}_{xx_{m1}} \\ \mathcal{E}_{yy_{m2}} \\ \mathcal{E}_{xy_{m3}} \end{bmatrix}, \tag{14a}$$

$$\mathcal{E}_n^k = \begin{bmatrix} \mathbf{N}_{m_1} & 0 & 0 \\ 0 & \mathbf{N}_{m_2} & 0 \\ 0 & 0 & 1 \end{bmatrix} \begin{bmatrix} \mathcal{E}_{xz_{m1}} \\ \mathcal{E}_{yz_{m2}} \\ \mathcal{E}_{zz} \end{bmatrix}. \tag{14b}$$

The subscripts m_1, m_2, and m_3 denote values that were assessed at each group's tying points. Using Eqs. (9a), (9b), the strain components at the tying sites, such as $\mathcal{E}_{xx_{m1}}$, must

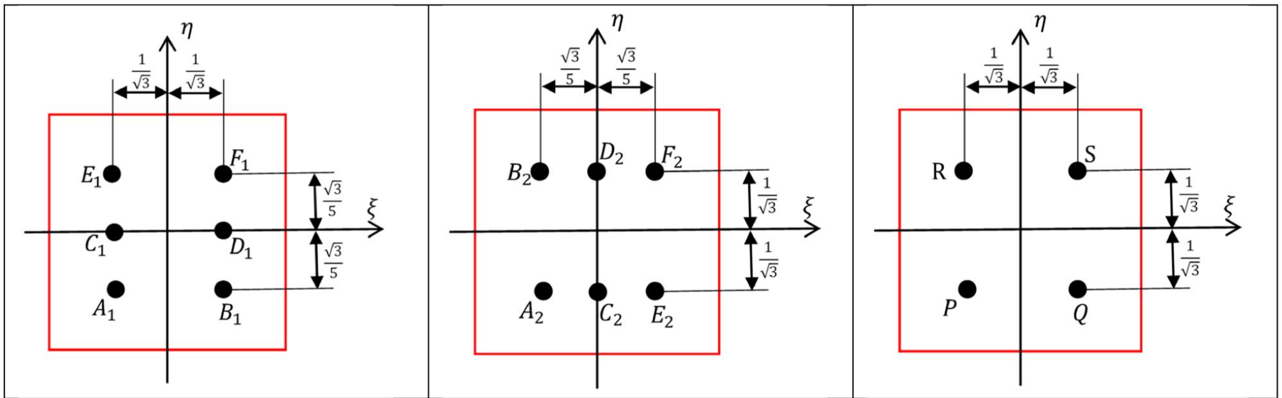

(a) Interpolation of $\mathcal{E}_{\mathbb{xx}}$ and $\mathcal{E}_{\mathbb{xz}}$ | (b) Interpolation of $\mathcal{E}_{\mathbb{yy}}$ and $\mathcal{E}_{\mathbb{yz}}$ | (c) Interpolation of $\mathcal{E}_{\mathbb{xy}}$.

Figure 4. MITC9 tying points for different strain components.

be directly estimated from the displacements. For instance, $\mathcal{E}_{\mathbb{xx}}$ becomes

$$\mathcal{E}_{\mathbb{xx}} = \mathcal{N}_{A1}\mathcal{E}_{\mathbb{xx}_{A_1}} + \mathcal{N}_{B1}\mathcal{E}_{\mathbb{xx}_{B_1}} + \mathcal{N}_{C1}\mathcal{E}_{\mathbb{xx}_{C_1}} + \mathcal{N}_{D1}\mathcal{E}_{\mathbb{xx}_{D_1}} + \mathcal{N}_{E1}\mathcal{E}_{\mathbb{xx}_{E_1}} + \mathcal{N}_{F1}\mathcal{E}_{\mathbb{xx}_{F_1}}, \tag{15}$$

where

$$\mathcal{E}_{\mathbb{xx}} = \mathcal{N}_{i,\mathbb{x}}^{(A1)} F_\tau \mathbb{u}_{\mathbb{x}\tau_i} + \frac{1}{\mathcal{H}_\mathbb{x} R_\mathbb{x}} \mathcal{N}_i^{(A1)} F_\tau \mathbb{u}_{\mathbb{z}\tau_i}. \tag{16}$$

The shape function and its derivative, $_{,\mathbb{x}}$, are evaluated at the location indicated by the superscript, A_1. The constitutive equations are defined with consideration for Hooke's law. Isolating in-plane and normal stress components for a composite material, it holds:

$$\sigma_p^k = \mathcal{C}_{pp}^k \mathcal{E}_p^k + \mathcal{C}_{pn}^k \mathcal{E}_n^k, \tag{17a}$$

$$\sigma_n^k = \mathcal{C}_{np}^k \mathcal{E}_p^k + \mathcal{C}_{nn}^k \mathcal{E}_n^k. \tag{17b}$$

The material coefficient matrices are defined as follows:

$$\mathcal{C}_{pp}^k = \begin{bmatrix} \mathcal{C}_{11}^k & \mathcal{C}_{12}^k & \mathcal{C}_{16}^k \\ \mathcal{C}_{12}^k & \mathcal{C}_{22}^k & \mathcal{C}_{26}^k \\ \mathcal{C}_{16}^k & \mathcal{C}_{26}^k & \mathcal{C}_{66}^k \end{bmatrix}, \mathcal{C}_{pn}^k = \begin{bmatrix} 0 & 0 & \mathcal{C}_{13}^k \\ 0 & 0 & \mathcal{C}_{23}^k \\ 0 & 0 & \mathcal{C}_{36}^k \end{bmatrix}, \tag{18a}$$

$$\mathcal{C}_{np}^k = \begin{bmatrix} 0 & 0 & 0 \\ 0 & 0 & 0 \\ \mathcal{C}_{13}^k & \mathcal{C}_{23}^k & \mathcal{C}_{36}^k \end{bmatrix}, \mathcal{C}_{nn}^k = \begin{bmatrix} \mathcal{C}_{55}^k & \mathcal{C}_{45}^k & 0 \\ \mathcal{C}_{45}^k & \mathcal{C}_{44}^k & 0 \\ 0 & 0 & \mathcal{C}_{33}^k \end{bmatrix}. \tag{18b}$$

where

$$\mathcal{C}_{11}^k(\mathbb{z}) = \mathcal{C}_{22}^k(\mathbb{z}) = \mathcal{C}_{33}^k(\mathbb{z}) = \frac{E^k(\mathbb{z})[1-(\nu^k(\mathbb{z}))^2]}{1-3(\nu^k(\mathbb{z}))^2 - 2(\nu^k(\mathbb{z}))^3}, \tag{19a}$$

$$\mathcal{C}_{12}^k(\mathbb{z}) = \mathcal{C}_{13}^k(\mathbb{z}) = \mathcal{C}_{23}^k(\mathbb{z}) = \frac{E^k(\mathbb{z})[\nu^k(\mathbb{z})-(\nu^k(\mathbb{z}))^2]}{1-3(\nu^k(\mathbb{z}))^2 - 2(\nu^k(\mathbb{z}))^3}, \tag{19b}$$

$$\mathcal{C}_{44}^k(\mathbb{z}) = \mathcal{C}_{55}^k(\mathbb{z}) = \mathcal{C}_{66}^k(\mathbb{z}) = \frac{E^k(\mathbb{z})}{2(1+\nu^k(\mathbb{z}))}, \tag{19c}$$

$$\mathcal{C}_{16}^k(\mathbb{z}) = \mathcal{C}_{26}^k(\mathbb{z}) = \mathcal{C}_{36}^k(\mathbb{z}) = \mathcal{C}_{45}^k(\mathbb{z}) = 0. \tag{19d}$$

The principle of virtual displacements (PVD) replaces constitutive and geometrical connections to produce the governing differential equations.

$$\delta L_{\text{int}} + \delta L_{\text{ext}} + \delta L_{\text{ine}} = 0. \tag{20}$$

The work performed by internal forces is denoted by L_{int}, the work performed by exterior forces by L_{ext}, and the inertial work by L_{ine}. In the case of free vibrations and a multilayered shell, Eq. (21) becomes:

$$\int_{\Omega_k}\int_{A_k} \delta\mathcal{E}^{k^T} \boldsymbol{\sigma}^k \mathcal{H}_\mathbb{x}^k \mathcal{H}_\mathbb{y}^k \mathrm{d}\Omega_k \mathrm{d}\mathbb{z} + \int_{\Omega_k}\int_{A_k} \rho^k \delta\mathbb{u}^{k^T} \ddot{\mathbb{u}}^k \mathcal{H}_\mathbb{x}^k \mathcal{H}_\mathbb{y}^k \mathrm{d}\Omega_k \mathrm{d}\mathbb{z} + \int_{\Omega_k}\int_{A_k} \delta\mathbb{u}^k \boldsymbol{p}^k \mathcal{H}_\mathbb{x}^k \mathcal{H}_\mathbb{y}^k \mathrm{d}\Omega_k \mathrm{d}\mathbb{z} = 0. \tag{21}$$

Ω_k and A_k denote the integration domains over $\mathbb{x}$, $\mathbb{y}$, and z, while ρ^k represents the mass density of the kth layer. The two dots represent acceleration, while T stands for vector transposition. The changes of the internal and inertial works may be recast as follows by changing the strains and stresses in Eq. (22) and using the FE formulation provided in Eq. (3) to describe the displacement field.

$$\delta L_{\text{int}}^k = \delta\mathbb{u}_{sj}^{k^T} \mathbf{k}^{k\tau sij} \mathbb{u}_{\tau i}^k, \tag{22a}$$

$$\delta L_{\text{ine}}^k = \delta\mathbb{u}_{sj}^{k^T} \mathbf{m}^{k\tau sij} \ddot{\mathbb{u}}_{\tau i}^k. \tag{22b}$$

where the stiffness and mass matrices, expressed as fundamental nuclei (FN), are denoted by the notations $\mathbf{k}^{k\tau sij}$ and $\mathbf{m}^{k\tau sij}$. FN, which are 3×3 arrays that function as fundamental assembly units, are theoretically unaffected by the structural theory's order.

$$\mathbf{k}^{k\tau sij} = \begin{bmatrix} k_{\mathbb{xx}}^{k\tau sij} & k_{\mathbb{xy}}^{k\tau sij} & k_{\mathbb{xz}}^{k\tau sij} \\ k_{\mathbb{yx}}^{k\tau sij} & k_{\mathbb{yy}}^{k\tau sij} & k_{\mathbb{yz}}^{k\tau sij} \\ k_{\mathbb{zx}}^{k\tau sij} & k_{\mathbb{zy}}^{k\tau sij} & k_{\mathbb{zz}}^{k\tau sij} \end{bmatrix}. \tag{23}$$

According to PVD, for a multi-layered shell that is exposed to external dynamic loadings:

$$\delta L_{\text{ext}} = \delta \mathbb{U}_{sj}^{k^T} \mathbf{p}^k. \tag{24}$$

where $\mathbf{T}^{\mathrm{T}} = \{ T_{\mathbb{x}} \quad T_{\mathbb{y}} \quad T_{\mathbb{z}} \}$ is the traction force acting over surface Ω. Refs. [62, 65] include the explicit formulations for each term of the basic nucleus of mass and stiffness. By iterating over the four indices (τ, s, i, j), the FE matrices may be produced. Depending on the modeling strategy taken into consideration, the matrices for each layer may be built after they are collected. This research only examined equivalent-single layer (ESL) models, which use a single set of unknown variables across the thickness, regardless of the structure's layer count. Finally, the free-vibration problem's governing equation may be reformulated as follows:

$$\mathbf{m}^{k\tau sij} \ddot{\boldsymbol{u}}_{\tau i} + \mathbf{k}^{k\tau sij} \mathbb{U}_{\tau i} = \mathbf{p}^k. \tag{25}$$

Applying Laplace transform [66] to Eq. (25) brings about the following relations

$$\mathbf{K}\hat{\mathbf{q}} + \mathbf{M}S^2\hat{\mathbf{q}} = \hat{\mathbf{P}}. \tag{26}$$

The layer-wise method combined with the Laplace transform to Eq. (26), yields the displacement for each layer. Using the modified formulation of Dubner and Abate, the displacements are calculated over time by using the inverse Laplace transform [66]. Therefore, Eq. (27) is the formula that was used in this work to carry out the inverse Laplace transform.

$$\zeta(t) = \frac{2e^{at}}{T}\left[-\frac{A_0}{2} + \sum_{k=0}^{\infty}\left(A_k \cos\left(\frac{2k\pi t}{T}\right) - B_k \sin\left(\frac{2k\pi t}{T}\right)\right)\right], \tag{27}$$

here

$$\begin{aligned} A_0 &= Re[F(a)], A_k = Re\left[F\left(a + i\frac{2k\pi}{T}\right)\right], \\ B_k &= Im\left[F\left(a + i\frac{2k\pi}{T}\right)\right], \end{aligned} \tag{28a}$$

$$S = a + i\frac{2k\pi}{T}, aT = 5. \tag{28b}$$

3. Introduction on artificial neural network to estimate dynamic analysis and structural integrity assessment of advanced nanocomposites reinforced tunnel structures

Artificial neural networks (ANNs) have emerged as a powerful tool for estimating the dynamic analysis and structural integrity assessment of advanced nanocomposite-reinforced tunnel structures. The complex behavior of such structures, particularly when reinforced with nanocomposite materials, requires sophisticated modeling techniques that can handle nonlinearity, material heterogeneity, and intricate load conditions [67, 68]. ANNs, inspired by the biological neural networks in the human brain, provide a computational framework that is well-suited for approximating these complex behaviors due to their ability to learn from data and generalize from limited information. Advanced nanocomposites, which incorporate nanoscale fillers such as carbon nanotubes or graphene into conventional materials, offer enhanced mechanical, thermal, and durability properties. These composites are becoming increasingly popular in tunnel structures due to their superior strength-to-weight ratio, high durability, and improved resistance to environmental factors. However, accurately predicting their performance under dynamic loads, such as seismic events or vehicular vibrations, presents significant challenges. Traditional finite element methods (FEM) and analytical solutions often fall short due to the high computational cost and difficulty in modeling the scale-dependent properties of nanomaterials. Here, ANNs provide a promising alternative. ANNs are highly effective in estimating complex structural responses by learning from past data. In the context of dynamic analysis, they can be trained using data from numerical simulations, or a combination of both. Once trained, ANNs can predict the dynamic response of nanocomposite-reinforced tunnel structures under various loading conditions, such as time-varying stresses and strains, without the need for repeated computationally expensive simulations. This capability makes ANNs a valuable tool for real-time assessment, especially for structures subjected to high-frequency loads or rapid changes in external conditions. In addition to dynamic analysis, ANNs are highly suitable for structural integrity assessments. The material properties of nanocomposites, particularly their dependence on nanoscale interactions and potential defects, make it challenging to predict failure modes and long-term performance using traditional methods. ANNs can be trained to recognize patterns that precede structural failure, such as micro-cracking or localized stress concentrations, enabling predictive maintenance and early warning systems for tunnel structures. By leveraging the pattern recognition and generalization capabilities of ANNs, engineers can estimate the performance and integrity of nanocomposite-reinforced tunnels more efficiently and accurately. This integration of ANN-based approaches into structural engineering offers a cost-effective and reliable method for enhancing the safety and longevity of critical infrastructure, particularly in regions prone to dynamic environmental loads such as earthquakes or heavy traffic. Figure 5 shows python code of the mentioned algorithm.

4. Results and discussion

4.1. Validation

Table 2 illustrates non-dimensional transversal displacement values at the top, middle, and bottom of a functionally graded (FG) plate under various conditions. Specifically, the displacements are calculated for different values of the FG power index (denoted by N) and aspect ratio (a/h), where a represents the width of the plate and h its thickness. The FG power index, N, defines how material properties vary through the thickness of the plate. A lower value of N implies a steeper material gradation, while higher values suggest a more uniform material distribution. The transversal displacement, is non-dimensional, meaning it has been normalized to allow for comparison across different configurations. The table provides these displacements

```
# Import required libraries
import numpy as np
import tensorflow as tf
from tensorflow.keras.models import Sequential
from tensorflow.keras.layers import Dense, Dropout
from sklearn.model_selection import train_test_split
from sklearn.preprocessing import StandardScaler
from sklearn.metrics import mean_squared_error
# Generate synthetic data for demonstration purposes
# In practice, you should replace this with actual simulation data
def generate_synthetic_data(samples=1000):
    np.random.seed(42)
    # Example input features: [load, thickness, composite_ratio, aspect_ratio]
    X = np.random.rand(samples, 4)
    # Simulated target dynamic responses: [displacement, stress]
    y = np.sum(X, axis=1) + 0.1 * np.random.randn(samples)  # Some simple relation for demo purposes
    return X, y
# Load the data (replace with your actual dataset)
X, y = generate_synthetic_data(samples=2000)
# Split the data into training and testing sets
X_train, X_test, y_train, y_test = train_test_split(X, y, test_size=0.2, random_state=42)
# Standardize the data (important for neural network performance)
scaler = StandardScaler()
X_train = scaler.fit_transform(X_train)
X_test = scaler.transform(X_test)
# Define the ANN model
def create_ann_model(input_dim):
    model = Sequential()
    model.add(Dense(64, activation='relu', input_dim=input_dim))  # First hidden layer
    model.add(Dense(32, activation='relu'))  # Second hidden layer
    model.add(Dense(16, activation='relu'))  # Third hidden layer
    model.add(Dense(1, activation='linear'))  # Output layer (for regression)
        # Compile the model
    model.compile(optimizer='adam', loss='mse', metrics=['mae'])
    return model
# Create the ANN model
model = create_ann_model(input_dim=X_train.shape[1])
# Train the model
history = model.fit(X_train, y_train, epochs=100, batch_size=32, validation_split=0.2, verbose=1)
# Evaluate the model on the test data
test_loss, test_mae = model.evaluate(X_test, y_test)
print(f'Test Loss (MSE): {test_loss}, Test MAE: {test_mae}')
# Make predictions on the test data
y_pred = model.predict(X_test)
# Calculate the Mean Squared Error on test data
mse = mean_squared_error(y_test, y_pred)
print(f'Mean Squared Error on test data: {mse}')
# Plot the training history (optional)
import matplotlib.pyplot as plt
plt.plot(history.history['loss'], label='Train Loss')
plt.plot(history.history['val_loss'], label='Validation Loss')
```

Figure 5. Python code of the mentioned algorithm.

at three points: the top, middle, and bottom surfaces of the plate. This offers a comprehensive view of how deformation is distributed through the plate's thickness under different conditions. The table is organized into three sections based on the aspect ratio, with values of 4, 10, and 50. As a/h increases, the plate becomes thinner relative to its width, which generally leads to larger displacements. The displacements are presented for two values of N, specifically $N = 3$ and $N = 4$, providing insight into how different material gradations affect the plate's deformation response. For lower aspect ratios, the

Table 2. Non-dimensional transversal displacement, calculated at the top, middle, and bottom of the plate for different FG power indexes (*N*) and a/h parameters.

	Ref. [69]	$N = 3$	$N = 4$
		$a/h = 4$	
$\bar{\mathcal{W}}(top)$	1.346×10^{-2}	1.348×10^{-2}	1.348×10^{-2}
$\bar{\mathcal{W}}(middle)$	1.370×10^{-2}	1.372×10^{-2}	1.372×10^{-2}
$\bar{\mathcal{W}}(bottom)$	1.273×10^{-2}	1.275×10^{-2}	1.275×10^{-2}
		$a/h = 10$	
$\bar{\mathcal{W}}(top)$	0.1689	0.1690	0.1690
$\bar{\mathcal{W}}(middle)$	0.1707	0.1708	0.1708
$\bar{\mathcal{W}}(bottom)$	0.1685	0.1686	0.1686
		$a/h = 50$	
$\bar{\mathcal{W}}(top)$	20.32	20.32	20.32
$\bar{\mathcal{W}}(middle)$	20.33	20.33	20.34
$\bar{\mathcal{W}}(bottom)$	20.32	20.32	20.32

displacements are relatively small, indicating that the plate is stiffer and resists deformation. As the aspect ratio increases to 50, the displacements increase significantly, reflecting the expected increase in flexibility for thinner plates. The nearly identical values for the top, middle, and bottom displacements suggest that the deformation is largely uniform through the thickness for high aspect ratios. This table helps engineers understand how material gradation and geometry influence the structural performance of FG plates in terms of their transverse deformation.

4.2. Parametric results

Figure 6 illustrates the dynamic response of a GOP (geometrically optimized) reinforced tunnel structure subjected to external loads. The graphs display the behavior of the tunnel's deformation and associated dynamic parameters, which are crucial for understanding its stability and performance under varying conditions. In the upper portion of the figure, the graph labeled a) $\mathcal{W}[m] - t[s]$ represents the vertical displacement (in meters) of the tunnel structure over time (in seconds). The three curves correspond to different GOP configurations: GOP-X (blue), GOP-O (yellow), and GOP-UD (red). Each configuration likely refers to specific geometric reinforcement patterns or boundary conditions applied to the structure. The graph indicates periodic oscillations in displacement, showing that the structure undergoes repeated deformation cycles, with each configuration exhibiting slightly different behavior in terms of amplitude and phase shift. This difference may be attributed to the varying reinforcement strategies influencing the tunnel's stiffness and dynamic response. In the second row, the subplots labeled b) $\frac{\partial \mathcal{W}}{\partial t}\left[\frac{m}{s}\right] - \mathcal{W}[m]$ provides further insight into the dynamic properties of the structure. The left subplot, b), shows the relationship between the time derivative of the displacement (velocity) and the displacement itself, depicting the velocity as a function of the vertical displacement. This graph helps in understanding the damping behavior and energy dissipation in the structure, indicating the velocity response with different GOP configurations. The right subplot, c), visualizes the acceleration response $\frac{\partial^2 \mathcal{W}}{\partial t^2}\left[\frac{m}{s^2}\right]$ against the velocity $\frac{\partial \mathcal{W}}{\partial t}\left[\frac{m}{s}\right]$. This graph provides essential information about the inertial forces acting on the structure and how it reacts dynamically under external excitations. The differences in the curves among GOP-X, GOP-O, and GOP-UD configurations highlight how varying reinforcement geometries influence the overall dynamic performance.

Figure 7 depicts the dynamic response of a GOP-reinforced structure, likely a tunnel, as influenced by different weight percentages of reinforcement materials. The graph is divided into three parts: a time-displacement plot, a velocity-displacement plot, and an acceleration-velocity plot, which together provide insight into the mechanical behavior of the structure under dynamic loading conditions. Figure 7a illustrates the vertical displacement of the structure over time, with four distinct curves corresponding to different reinforcement material percentages: $W_{GOP} = 0.1[wt\%]$, $W_{GOP} = 0.2[wt\%]$, $W_{GOP} = 0.3[wt\%]$, and $W_{GOP} = 0.4\ [wt\%]$. These percentages represent the concentration of the reinforcement material in the tunnel structure. As expected, each curve exhibits periodic oscillations, with the amplitude and phase of the oscillations varying depending on the weight percentage of the reinforcement. The variation indicates that the structure's stiffness, damping, and dynamic properties are directly affected by the reinforcement material concentration. Notably, the structure with the lowest weight percentage ($W_{GOP} = 0.1[wt\%]$) seems to show the largest displacement, suggesting a more flexible or less stiff configuration, while higher percentages like $W_{GOP} = 0.4[wt\%]$ demonstrate a reduced amplitude of oscillation, indicating increased stiffness. Figure 7b illustrates the relationship between the velocity (the time derivative of displacement) and the displacement itself. The closed-loop curves indicate a periodic system where velocity varies with displacement in a cyclical manner. The differing shapes of the loops for each reinforcement percentage show how the structure's velocity response changes with the reinforcement concentration. Generally, the curves with higher reinforcement percentages display more compressed loops, reflecting reduced velocity variations and more controlled oscillations, which are typical of stiffer systems. Figure 6c shows the relationship between acceleration (the second time derivative of displacement) and velocity. The nested loops provide a deeper understanding of how inertia influences the structure's dynamic response. Similar to the

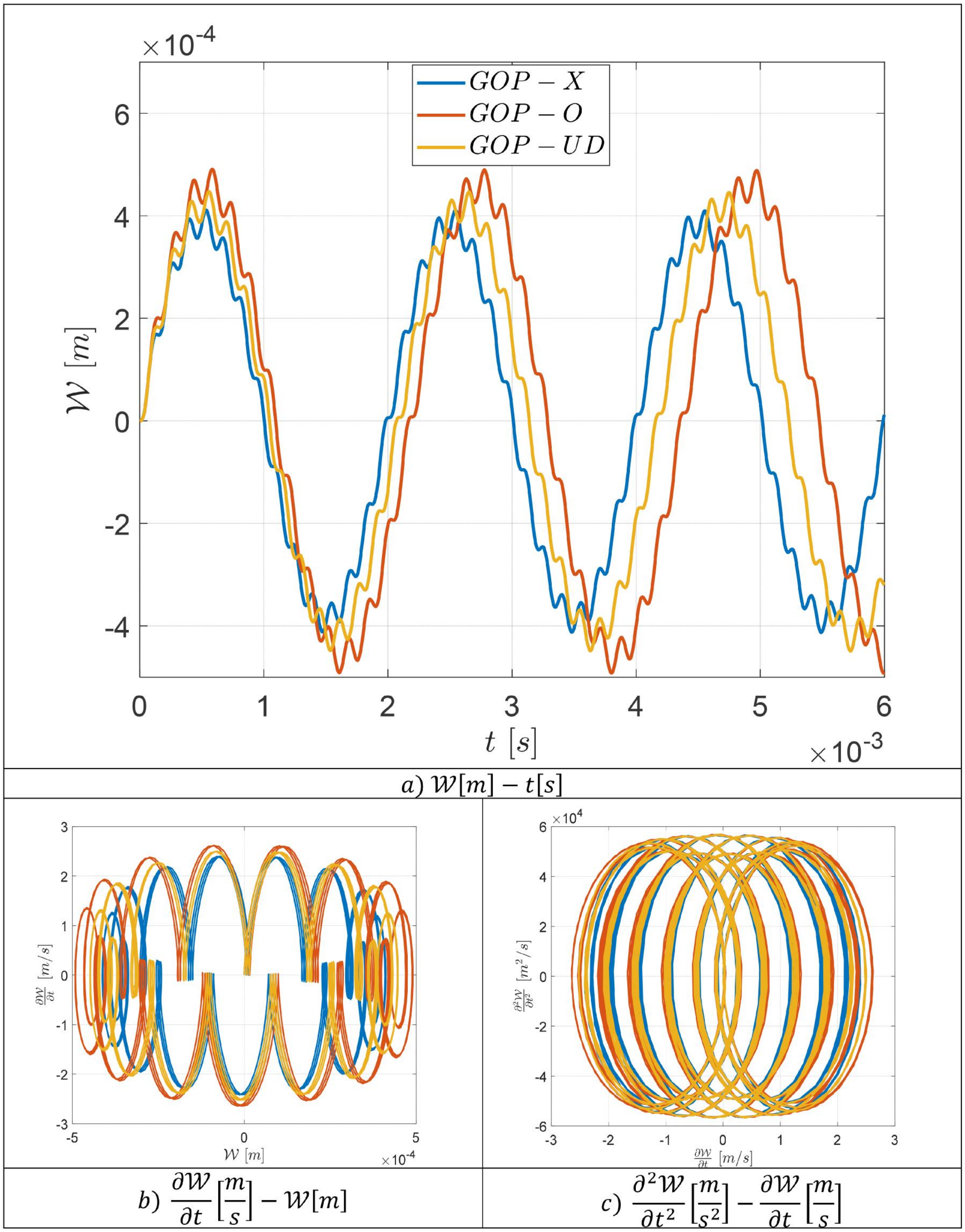

Figure 6. Dynamical properties of GOP reinforced tunnel structures for various GOP distribution patterns.

velocity–displacement plot, the variations in the shapes of these loops with different reinforcement concentrations indicate how the material properties affect the tunnel's inertial and damping behavior. The higher weight percentages of reinforcement materials result in more stable, narrower loops, suggesting enhanced damping and reduced inertial effects compared to the lower weight percentage cases. In summary, this figure highlights how the dynamic characteristics of the GOP-reinforced tunnel, including displacement, velocity, and acceleration, are influenced by the weight percentage of the reinforcement material, with higher concentrations leading to increased stiffness and reduced dynamic response.

Figure 8 illustrates the dynamic response of a GOP reinforced tunnel structure under harmonic loading conditions. The top graph (a) represents the displacement the structure over time, showing how the tunnel reacts to four different magnitudes of external harmonic forces, each with increasing amplitudes proportional. The loading function is defined as $F(t) = P_0 \times \sin(\Omega_{ext} \times t)$, where P_0 is a force parameter,

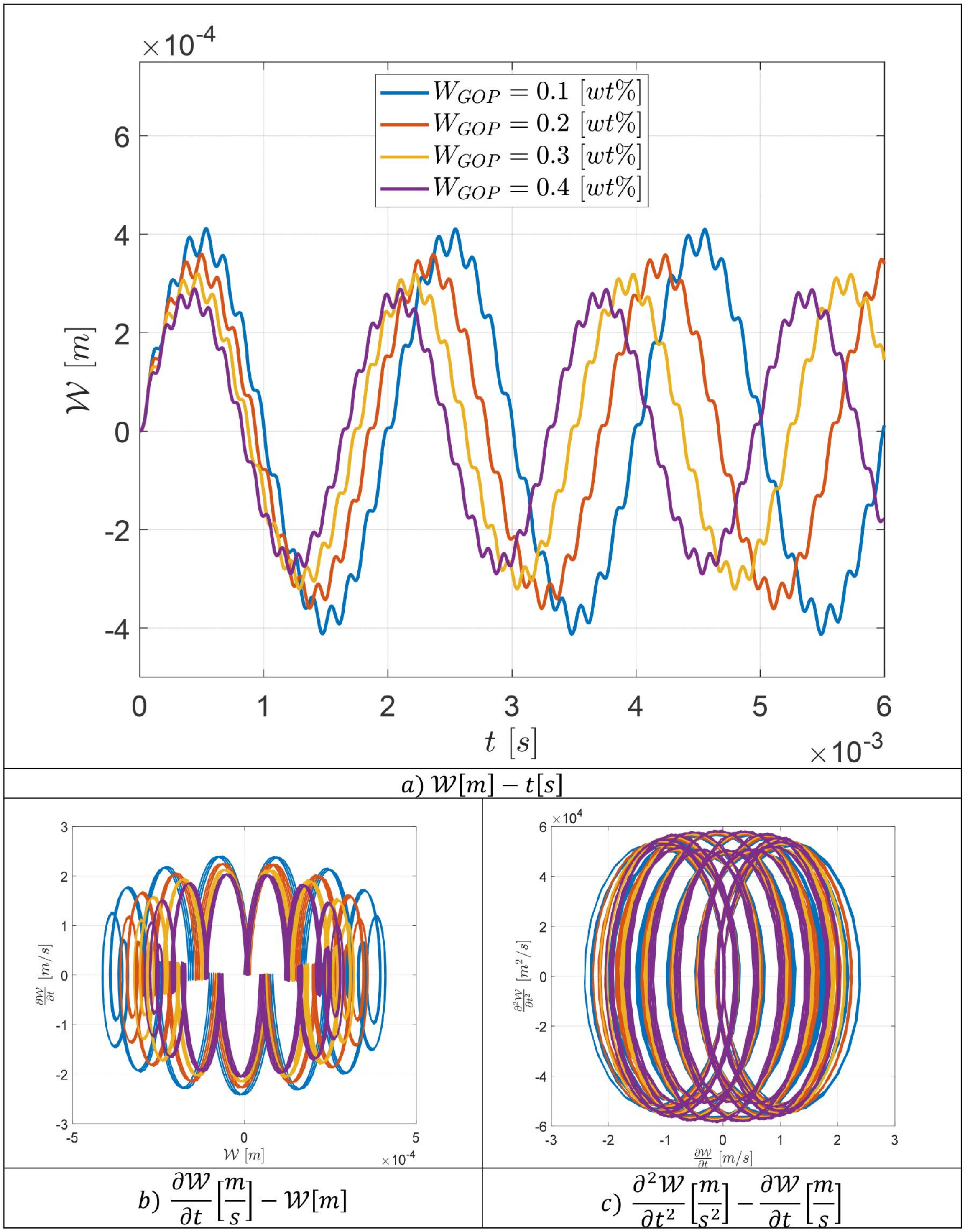

Figure 7. Dynamical properties of GOP reinforced tunnel structures for various GOP weight fractions.

and Ω_{ext} is the excitation frequency. The color-coded curves indicate the displacement variations for P_0, $1.5P_0$, $2P_0$, and $2.5P_0$, which shows how higher forces result in increased oscillation amplitude while maintaining a similar periodicity. The bottom left graph (b) shows the phase-space diagram, plotting the relationship between the displacement and its time derivative. The closed-loop, oval-shaped trajectories in this diagram indicate stable periodic motion, where the structural response is governed by nonlinear vibration characteristics. The bottom right graph (c) presents the relationship between displacement and its second derivative, highlighting the structural acceleration as a function of displacement. The intricate loops suggest that as the structure undergoes larger displacements, it experiences nonlinear dynamic effects due to the geometric and material properties of the GOP reinforcement. Together, these plots provide a comprehensive view of the structure's dynamic behavior under varying harmonic loads, emphasizing the interplay between force amplitude, displacement, velocity, and acceleration. This information is crucial for understanding and

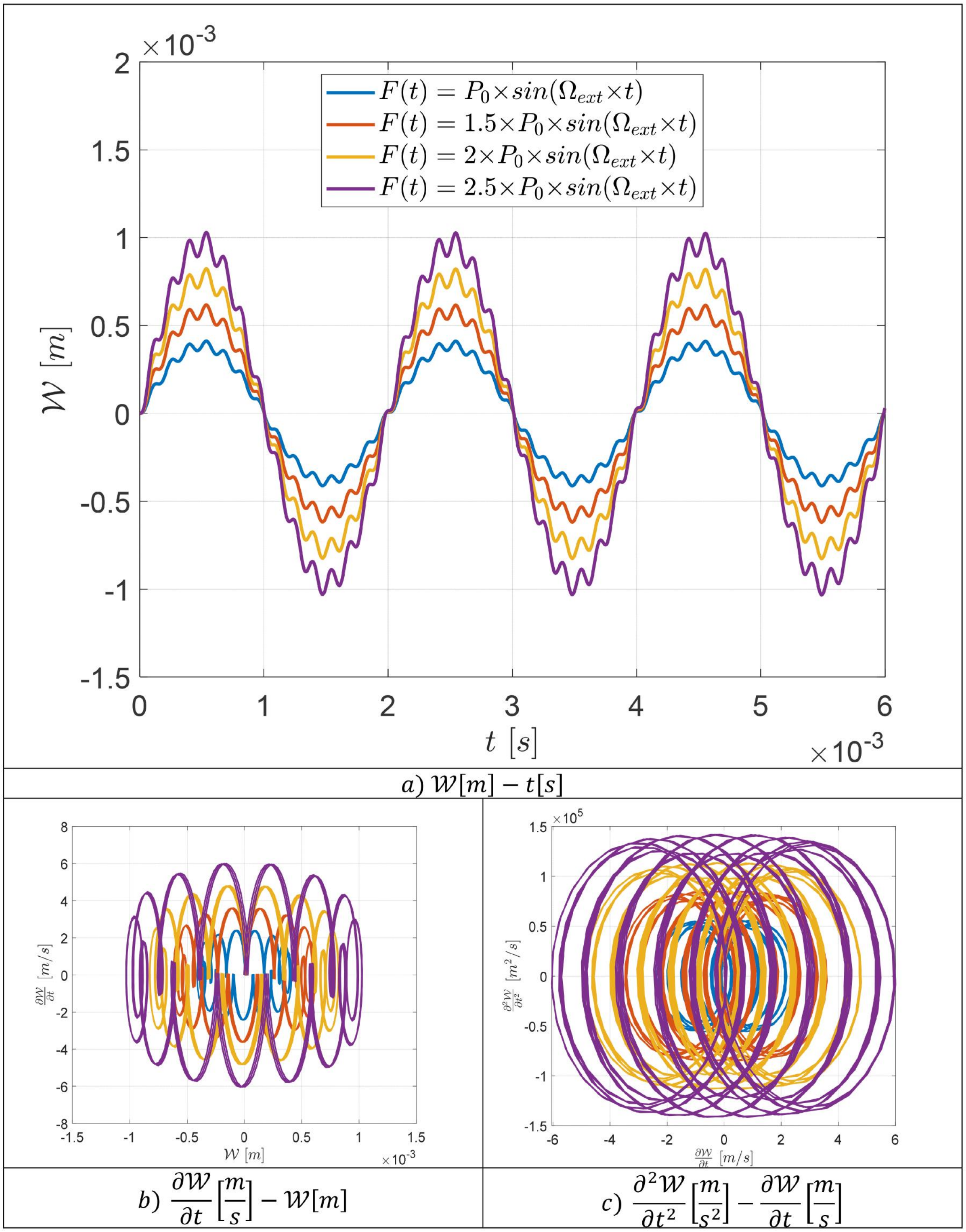

Figure 8. Dynamical properties of GOP reinforced tunnel structures for various external loading's distribution patterns.

designing resilient tunnel structures with graphene reinforcement.

Figure 9 presents the dynamic response of a graphene oxide platelet reinforced tunnel structure, with varying structural geometries characterized by different ratios of R_1/a. The top graph (a) illustrates the displacement over time for four different geometric configurations: $R_1/a = 10$, 20, 30, and 40. These variations represent changes in the stiffness and curvature of the tunnel structure, with higher ratios indicating a flatter configuration. As the ratio increases, the displacement profile shows higher amplitudes and more complex behavior, implying greater sensitivity to external forces. The bottom left graph (b) shows phase-space diagrams of displacement versus its first time derivative, which reflect the system's velocity response. The closed-loop curves are indicative of periodic, nonlinear oscillations, with the larger ratios leading to larger phase-space loops, denoting more significant energy exchange between kinetic and potential states. The bottom right graph (c) presents the relationship between displacement and the second derivative,

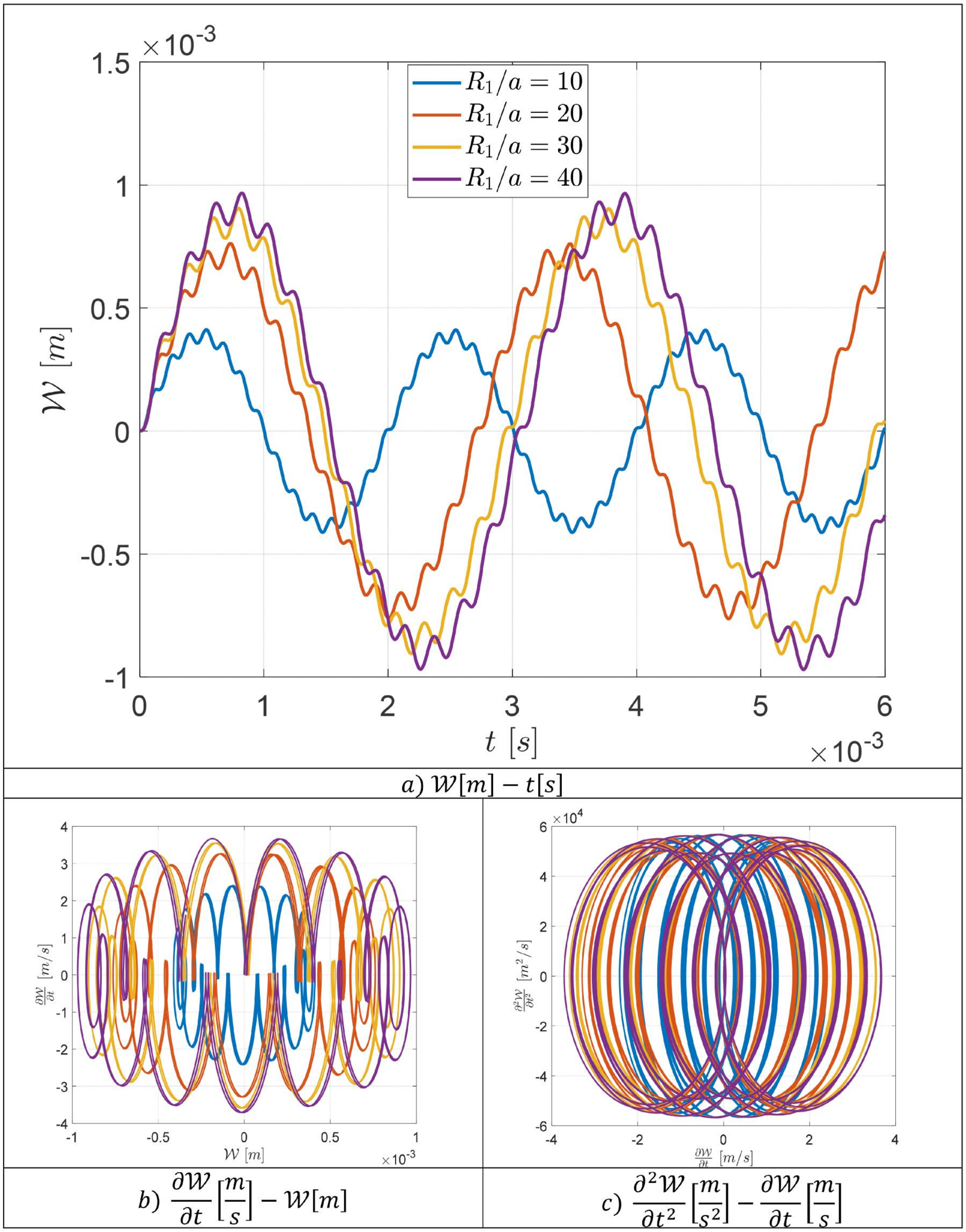

Figure 9. Dynamical properties of GOP reinforced tunnel structures for various R_1/a parametrs.

representing acceleration. The nested, complex loops signify nonlinear dynamic effects, where higher R_1/a ratios result in broader, more intricate oscillatory patterns. These loops highlight the nonlinear stiffness and damping characteristics influenced by the GOP reinforcement and the geometric configuration. This analysis is critical for optimizing tunnel structures, as it provides insight into the effects of curvature and material properties on vibration behavior under external forces.

Figure 10 shows the dynamic response of a graphene oxide platelet reinforced tunnel structure under varying excitation frequencies. The top graph (a) represents the displacement as a function of time, subject to external harmonic forces with four different excitation frequencies: $\Omega_{ext}=0.15\times\omega_{11},\ 0.3\times\omega_{11},\ 0.45\times\omega_{11},$ and $0.6\times\omega_{11}$, where ω_{11} is a reference frequency. As the excitation frequency increases, the displacement amplitudes also increase, reflecting stronger resonant effects. At higher frequencies

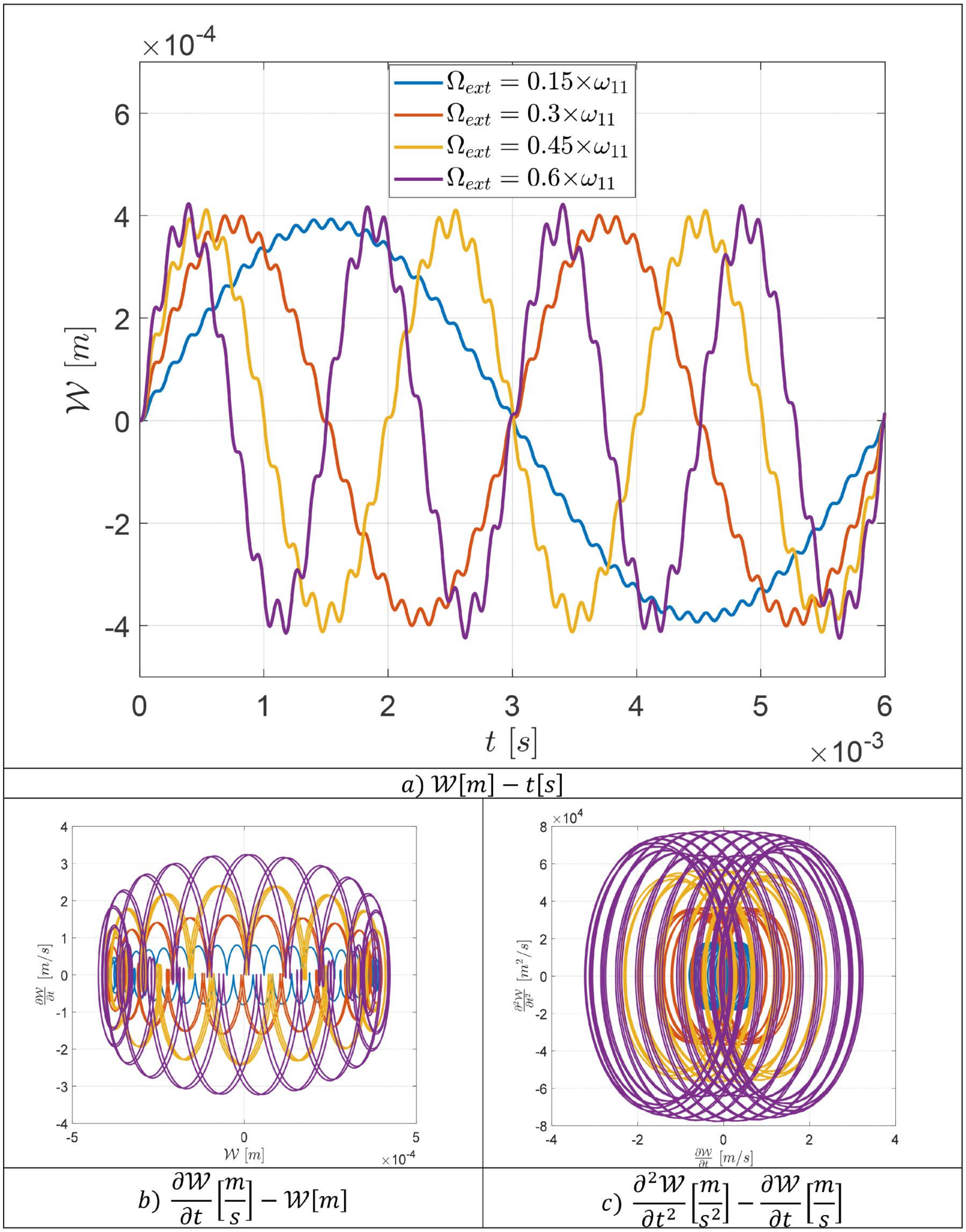

Figure 10. Dynamical properties of GOP reinforced tunnel structures for various Ω_{ext} parametrs.

$\Omega_{ext} = 0.45 \times \omega_{11}$ and $\Omega_{ext} = 0.6 \times \omega_{11}$, the response becomes more complex, showing increased oscillation irregularities due to nonlinear dynamic effects and possible proximity to resonance. The bottom left graph (b) shows the phase-space trajectories, plotting displacement against its time derivative, or velocity. These closed-loop trajectories indicate periodic motion, where higher excitation frequencies result in wider loops, signifying larger velocities and more energetic oscillations. The bottom right graph (c) presents the relationship between displacement and the second time derivative, representing acceleration. As in the phase-space diagram, the loops in this plot show that higher excitation frequencies lead to more pronounced nonlinear effects, with the loops becoming increasingly intricate. This indicates greater structural acceleration with larger displacements under higher excitation frequencies, pointing to complex interaction between the GOP reinforcement and the external forces. This analysis is vital for understanding how

Table 3. An analysis of the DNN model's performance for dynamic deflection at different.

W_{GOP} and RMSN values

W_{GOP} ($wt\%$)	Fit	Predicted $RMSE_{Train}=0.19$	$RMSE_{Train}=0.23$	$RMSE_{Train}=0.28$
0.4	2.596	2.36236	2.49216	2.58302
0.3	2.912	2.64992	2.79552	2.89744
0.2	3.315	3.01665	3.1824	3.298425
0.1	3.658	3.32878	3.51168	3.63971
0	4.125	3.75375	3.96	4.104375

Table 4. Performance of the DNN model's performance for dynamic deflection is evaluated across several values of R^2 and W_{GOP}.

W_{GOP} ($wt\%$)	Fit	Predicted R^2=0.7952	R^2=0.8362	R^2=0.9152
0.4	2.596	2.38832	2.51812	2.58302
0.3	2.912	2.67904	2.82464	2.89744
0.2	3.315	3.0498	3.21555	3.298425
0.1	3.658	3.36536	3.54826	3.63971
0	4.125	3.795	4.00125	4.104375

varying excitation frequencies impact the dynamic behavior of GOP-reinforced tunnel structures, particularly in terms of stability, resonance, and energy dissipation.

4.3. The results of mentioned algorithm

Now the trained results of the offered deep neural networks are generated by using the previously discussed benefits and the outcomes of mathematical modeling. To evaluate the efficacy of the model, the present study examines five statistical variables, including root mean square error (RMSE) and coefficient of determination (R^2). Here are a few ways to find out who they are:

$$R^2=\frac{\sum_{i=1}^{N}(O_i-O_{avg})^2-\sum_{i=1}^{N}(O_i-y_i)^2}{\sum_{i=1}^{N}(O_i-O_{avg})^2}, \tag{29a}$$

$$RMSE=\sqrt{\frac{1}{N}\sum_{i=1}^{N}(O_i-y_i)^2}, \tag{29b}$$

The Ref. provides a thorough explanation of the parameters used in Eqs. (29a) and (29b) [70]. Using Tables 3 and 4, this section examines how R^2 and RMSE affect the outcomes. One may presume that a response with greater R^2 and RMSE parameter values is more accurate. It is quite helpful to have chosen 691 samples with RMSE = 0.28, R^2 =0.9152, and other values.

Tables 3 and 4 show that for both the numerical and DNN approaches, the structure's dynamic deflection decreases as the W_{GOP} increases.

5. Conclusion

The results presented in this study demonstrate the effectiveness of the CUF for the dynamic analysis and structural integrity assessment of advanced nanocomposite-reinforced tunnel structures. CUF, with its ability to account for higher-order theories and complex material behaviors, provides an accurate and versatile tool for engineers when modeling such structures. The formulation's flexibility, particularly in handling multi-scale phenomena and diverse structural configurations, makes it a reliable approach for assessing the performance of nanocomposites under dynamic loading conditions, which is often challenging for traditional modeling techniques. The inherent complexity of nanocomposite materials, with their tailored properties and material gradation, requires advanced modeling capabilities that CUF addresses through its generalization and comprehensive framework. Moreover, the integration of ANNs in this study further validates the robustness of CUF-based predictions. By training an ANN with simulation data, we were able to create a powerful hybrid approach that improves the accuracy and computational efficiency of dynamic analysis. The ANN's ability to learn from data and generalize responses allows for real-time prediction of the structure's behavior under varying load conditions. This enables rapid assessment of tunnel structures, making the approach highly suitable for practical applications, where time and computational resources may be limited. The combination of CUF and ANN is thus shown to be highly advantageous in structural integrity assessments, where quick and reliable predictions are necessary, especially for critical infrastructure such as tunnels. The study also highlights the potential of this integrated approach for applications in various fields beyond tunnel structures. The CUF-ANN methodology can be extended to other civil, aerospace, and mechanical engineering domains, where advanced composite materials are used and dynamic behavior is of concern. Additionally, the success of this approach in modeling complex systems opens doors for further exploration into other machine learning techniques that can complement high-order structural theories. In conclusion, the integration of CUF and ANN provides a powerful, efficient, and reliable method for the dynamic analysis and structural integrity assessment of nanocomposite-reinforced tunnel structures. This framework has the potential to significantly advance the field of structural analysis, especially in applications requiring both precision and speed.

Disclosure statement

No potential conflict of interest was reported by the author(s).

Funding

This work was supported by the Science and Technology Research Program of Chongqing Municipal Education Commission (Grant No. KJZD-K202303403). The authors extend their appreciation to King Saud University, Saudi Arabia for funding this work through Researchers Supporting Project number (RSP2024R305), King Saud University, Riyadh, Saudi Arabia.

References

[1] E. Mohseni, A.R. Saidi, and M. Mohammadi, Bending-stretching analysis of thick functionally graded micro-plates using higher-order shear and normal deformable plate theory, Mech.

Adv. Mater. Struct., vol. 24, no. 14, pp. 1221–1230, 2017. DOI: 10.1080/15376494.2016.1227503.

[2] H.-S. Shen, X.-H. Huang, and J. Yang, Nonlinear bending of temperature-dependent FG-CNTRC laminated plates with negative Poisson's ratio, Mech. Adv. Mater. Struct., vol. 27, no. 13, pp. 1141–1153, 2020. DOI: 10.1080/15376494.2020.1716412.

[3] Z.-Z. Wang, T. Wang, Y-m Ding, and L-s Ma, A simple refined plate theory for the analysis of bending, buckling and free vibration of functionally graded porous plates reinforced by graphene platelets, Mech. Adv. Mater. Struct., vol. 31, no. 8, pp. 1699–1716, 2024. DOI: 10.1080/15376494.2022.2141383.

[4] A.G. Chanda, and D. Punera, Porosity-dependent free vibration and transient responses of functionally graded composite plates employing higher order thickness stretching model, Mech. Adv. Mater. Struct., vol. 31, no. 7, pp. 1491–1516, 2024. DOI: 10.1080/15376494.2022.2138652.

[5] C. Lin, G. Pan, and M. Abbas, Introducing ANN-GP algorithm to estimate transient bending of the functionally graded graphene origami-enabled auxetic metamaterial structures, Mech. Adv. Mater. Struct., pp. 1–20, 2024. DOI: 10.1080/15376494.2024.2344020.

[6] J. Najd, E. Zappino, E. Carrera, W. Harizi, and Z. Aboura, Optimal position and dimensions of embedded normal piezoelectric transducers, higher order plate models and experimental approach, Mech. Adv. Mater. Struct., pp. 1–12, 2024. DOI: 10.1080/15376494.2024.2342028.

[7] E. Carrera, and V.V. Zozulya, Carrera unified formulation (CUF) for the shells of revolution. Numerical evaluation, Mech. Adv. Mater. Struct., vol. 31, no. 7, pp. 1597–1619, 2024. DOI: 10.1080/15376494.2022.2140234.

[8] E. Carrera, Theories and finite elements for multilayered plates and shells: a unified compact formulation with numerical assessment and benchmarking, ARCO, vol. 10, no. 3, pp. 215–296, 2003. DOI: 10.1007/BF02736224.

[9] A.M.A. Neves, A.J.M. Ferreira, E. Carrera, M. Cinefra, R.M.N. Jorge, and C.M.M. Soares, Buckling analysis of sandwich plates with functionally graded skins using a new quasi-3D hyperbolic sine shear deformation theory and collocation with radial basis functions, Z. Angew. Math. Mech., vol. 92, no. 9, pp. 749–766, 2012. DOI: 10.1002/zamm.201100186.

[10] A. Belounar, S. Benmebarek, and L. Belounar, Strain based triangular finite element for plate bending analysis, Mech. Adv. Mater. Struct., vol. 27, no. 8, pp. 620–632, 2020. DOI: 10.1080/15376494.2018.1488310.

[11] S.-R. Li, F. Zhang, and R.-G. Liu, Classical and homogenized expressions for the bending solutions of FGM plates based on the four variable plate theories, Mech. Adv. Mater. Struct., vol. 31, no. 15, pp. 3413–3424, 2024. DOI: 10.1080/15376494.2023.2177909.

[12] Z. Zhong, S. Chen, and E. Shang, Analytical solution of a functionally graded plate in cylindrical bending, Mech. Adv. Mater. Struct., vol. 17, no. 8, pp. 595–602, 2010. DOI: 10.1080/15376494.2010.517729.

[13] K. Bendine, F.B. Boukhoulda, B. Haddag, and M. Nouari, Active vibration control of composite plate with optimal placement of piezoelectric patches, Mech. Adv. Mater. Struct., vol. 26, no. 4, pp. 341–349, 2019. DOI: 10.1080/15376494.2017.1387324.

[14] M. Burkov, and A. Eremin, Evaluation of fracture toughness of hybrid CNT/CFRP composites, Mech. Adv. Mater. Struct., vol. 30, no. 14, pp. 2872–2881, 2023. DOI: 10.1080/15376494.2022.2064569.

[15] R. Augello and E. Carrera, Analysis of plate reinforced by straight and curved stiffeners by using novel plate elements with refined through-the-thickness expansion, Mech. Adv. Mater. Struct., vol. 31, pp. 1–4, 2023. DOI: 10.1080/15376494.2023.2270794.

[16] E. Carrera, M. Didem Demirbas, and R. Augello, Evaluation of stress distribution of isotropic, composite, and FG beams with different geometries in nonlinear regime via Carrera-unified formulation and Lagrange polynomial expansions, Appl. Sci., vol. 11, no. 22, pp. 10627, 2021. DOI: 10.3390/app112210627.

[17] E. Carrera, F. Miglioretti, and M. Petrolo, Accuracy of refined finite elements for laminated plate analysis, Compos. Struct., vol. 93, no. 5, pp. 1311–1327, 2011. DOI: 10.1016/j.compstruct.2010.11.007.

[18] F. Boumediene, E.M. Daya, J.-M. Cadou, and L. Duigou, Forced harmonic response of viscoelastic sandwich beams by a reduction method, Mech. Adv. Mater. Struct., vol. 23, no. 11, pp. 1290–1299, 2016. DOI: 10.1080/15376494.2015.1068408.

[19] E. Carrera, Transverse normal strain effect on thermal stress analysis of homogeneous and layered plates, AIAA J., vol. 43, no. 10, pp. 2232–2242, 2005. DOI: 10.2514/1.11230.

[20] D. Hu, H. Sun, P. Mehrabi, Y.A. Ali, and M. Al-Razgan, Application of artificial intelligence technique in optimization and prediction of the stability of the walls against wind loads in building design, Mech. Adv. Mater. Struct., vol. 31, no. 19, pp. 4755–4772, 2024. DOI: 10.1080/15376494.2023.2206208.

[21] J. Wu, Y. Yang, P. Mehrabi, and E.A. Nasr, Efficient machine-learning algorithm applied to predict the transient shock reaction of the elastic structure partially rested on the viscoelastic substrate, Mech. Adv. Mater. Struct., vol. 31, no. 16, pp. 3700–3724, 2024. DOI: 10.1080/15376494.2023.2183289.

[22] E. Carrera, Mixed layer-wise models for multilayered plates analysis, Compos. Struct., vol. 43, no. 1, pp. 57–70, 1998. DOI: 10.1016/S0263-8223(98)00097-X.

[23] E. Carrera, A class of two-dimensional theories for anisotropic multilayered plates analysis. In: Atti Della Accademia Delle Scienze Di Torino. Classe Di Scienze Fisiche Matematiche e Naturali, vol. 19, pp. 1–39, 1995.

[24] M.H. Amini, M. Soleimani, A. Altafi, and A. Rastgoo, Effects of geometric nonlinearity on free and forced vibration analysis of moderately thick annular functionally graded plate, Mech. Adv. Mater. Struct., vol. 20, no. 9, pp. 709–720, 2013. DOI: 10.1080/15376494.2012.676711.

[25] A. Robaldo, E. Carrera, and A. Benjeddou, A unified formulation for finite element analysis of piezoelectric adaptive plates, Comput. Struct., vol. 84, no. 22–23, pp. 1494–1505, 2006.

[26] E. Carrera, Developments, ideas, and evaluations based upon Reissner's mixed variational theorem in the modeling of multilayered plates and shells, Appl. Mech. Rev., vol. 54, no. 4, pp. 301–329, 2001. DOI: 10.1115/1.1385512.

[27] E. Carrera, Historical review of zig-zag theories for multilayered plates and Shells, Appl. Mech. Rev., vol. 56, no. 3, pp. 287–308, 2003. DOI: 10.1115/1.1557614.

[28] E. Carrera, and V.V. Zozulya, Carrera Unified Formulation (CUF) for the micropolar plates and shells. I. Higher order theory, Mech. Adv. Mater. Struct., vol. 29, no. 6, pp. 773–795, 2022. DOI: 10.1080/15376494.2020.1793241.

[29] E. Carrera, and V.V. Zozulya, Carrera unified formulation for the micropolar plates, Mech. Adv. Mater. Struct., vol. 29, no. 22, pp. 3163–3186, 2022. DOI: 10.1080/15376494.2021.1889726.

[30] E. Carrera and V. Zozulya, Carrera Unified Formulation (CUF) for the Composite Plates and Shells of Revolution. Layer-Wise Models, Comput. Struct., p. 117936, 2024.

[31] V.V. Zozulya, and E. Carrera, Carrera unified formulation (CUF) for the micropolar plates and shells. III. Classical models, Mech. Adv. Mater. Struct., vol. 29, no. 27, pp. 6336–6360, 2022. DOI: 10.1080/15376494.2021.1975855.

[32] E. Carrera, and V.V. Zozulya, Carrera unified formulation (CUF) for the composite shells of revolution. Equivalent single layer models, Mech. Adv. Mater. Struct., vol. 31, no. 1, pp. 22–44, 2024c. DOI: 10.1080/15376494.2023.2218380.

[33] W. Wei, J. Gong, J. Deng, and W. Xu, Effects of air vent size and location design on air supply efficiency in flood discharge tunnel operations, J. Hydraul. Eng., vol. 149, no. 12, pp. 04023050, 2023. DOI: 10.1061/JHEND8.HYENG-13305.

[34] W. Wei, W. Xu, J. Deng, and Y. Guo, Self-aeration development and fully cross-sectional air diffusion in high-speed open

channel flows, J. Hydraul. Res., vol. 60, no. 3, pp. 445–459, 2022. DOI: 10.1080/00221686.2021.2004250.

[35] K. Ma, Y. Peng, Z. Liao, and Z. Wang, Dynamic responses and failure characteristics of the tunnel caused by rockburst: an entire process modelling from incubation to occurrence phases, Comput. Geotech., vol. 171, pp. 106340, 2024. DOI: 10.1016/j.compgeo.2024.106340.

[36] R. Yao, Z. Ge, D. Wang, N. Shang, and J. Shi, Self-sensing joints for in-situ structural health monitoring of composite pipes: a piezoresistive behavior-based method, Eng. Struct., vol. 308, pp. 118049, 2024. DOI: 10.1016/j.engstruct.2024.118049.

[37] M. Shi, W. Hu, M. Li, J. Zhang, X. Song, and W. Sun, Ensemble regression based on polynomial regression-based decision tree and its application in the in-situ data of tunnel boring machine, Mech. Syst. Sig. Process., vol. 188, pp. 110022, 2023. DOI: 10.1016/j.ymssp.2022.110022.

[38] M-m Sun, H-y Fang, N-n Wang, X-m Du, H-s Zhao, and K.-J. Zhai, Limit state equation and failure pressure prediction model of pipeline with complex loading, Nat. Commun., vol. 15, no. 1, pp. 4473, 2024. DOI: 10.1038/s41467-024-48688-1.

[39] L.-C. Deng, W. Zhang, L. Deng, Y.-H. Shi, J.-J. Zi, X. He, and H.-H. Zhu, Forecasting and early warning of shield tunnelling-induced ground collapse in rock-soil interface mixed ground using multivariate data fusion and catastrophe theory, Eng. Geol., vol. 335, pp. 107548, 2024. DOI: 10.1016/j.enggeo.2024.107548.

[40] B. Zou, J. Yin, Z. Liu, and X. Long, Transient rock breaking characteristics by successive impact of shield disc cutters under confining pressure conditions, Tunnel. Undergr. Space Technol., vol. 150, pp. 105861, 2024. DOI: 10.1016/j.tust.2024.105861.

[41] J. Wang, S.-Q. Lin, D.-Y. Tan, J.-H. Yin, H.-H. Zhu, and S.C. Kuok, A novel method for integrity assessment of soil-nailing works with actively heated fiber-optic sensors, J. Geotech. Geoenviron. Eng., vol. 150, no. 8, pp. 04024063, 2024. DOI: 10.1061/JGGEFK.GTENG-11790.

[42] W. Zhang, S. Kang, X. Liu, B. Lin, and Y. Huang, Experimental study of a composite beam externally bonded with a carbon fiber-reinforced plastic plate, J. Build. Eng., vol. 71, pp. 106522, 2023. DOI: 10.1016/j.jobe.2023.106522.

[43] H. Khorshidi, C. Zhang, E. Najafi, and M. Ghasemi, Fresh, mechanical and microstructural properties of alkali-activated composites incorporating nanomaterials: a comprehensive review, J. Cleaner Prod., vol. 384, pp. 135390, 2023. DOI: 10.1016/j.jclepro.2022.135390.

[44] B. Liu, H. Yang, and S. Karekal, Effect of water content on argillization of mudstone during the tunnelling process, Rock Mech. Rock Eng., vol. 53, no. 2, pp. 799–813, 2020. DOI: 10.1007/s00603-019-01947-w.

[45] H. Yang, C. Chen, J. Ni, and S. Karekal, A hyperspectral evaluation approach for quantifying salt-induced weathering of sandstone, Sci. Total Environ., vol. 885, pp. 163886, 2023. DOI: 10.1016/j.scitotenv.2023.163886.

[46] H. Yang, K. Song, and J. Zhou, Automated recognition model of geomechanical information based on operational data of tunneling boring machines, Rock Mech. Rock Eng., vol. 55, no. 3, pp. 1499–1516, 2022. DOI: 10.1007/s00603-021-02723-5.

[47] C. Chen, H. Yang, K. Song, D. Liang, Y. Zhang, and J. Ni, Dissolution feature differences of carbonate rock within hydro-fluctuation belt located in the three gorges reservoir area, Eng. Geol., vol. 327, pp. 107362, 2023. DOI: 10.1016/j.enggeo.2023.107362.

[48] H. Yang, J. Ni, C. Chen, and Y. Chen, Weathering assessment approach for building sandstone using hyperspectral imaging technique, Herit. Sci., vol. 11, no. 1, pp. 70, 2023. DOI: 10.1186/s40494-023-00914-7.

[49] K. Song, H. Yang, D. Liang, L. Chen, and M. Jaboyedoff, Step-like displacement prediction and failure mechanism analysis of slow-moving reservoir landslide, J. Hydrol., vol. 628, pp. 130588, 2024. DOI: 10.1016/j.jhydrol.2023.130588.

[50] S. Han, D. Zheng, B. Mehdizadeh, E.A. Nasr, M.U. Khandaker, M. Salman, and P. Mehrabi, Sustainable design of self-consolidating green concrete with partial replacements for cement through neural-network and fuzzy technique, Sustainability, vol. 15, no. 6, pp. 4752, 2023. DOI: 10.3390/su15064752.

[51] S. Han, Z. Zhu, M. Mortazavi, A.M. El-Sherbeeny, and P. Mehrabi, Analytical assessment of the structural behavior of a specific composite floor system at elevated temperatures using a newly developed hybrid intelligence method, Buildings, vol. 13, no. 3, pp. 799, 2023. DOI: 10.3390/buildings13030799.

[52] E. Taheri, P. Mehrabi, S. Rafiei, and B. Samali, Numerical evaluation of the upright columns with partial reinforcement along with the utilisation of neural networks with combining feature-selection method to predict the load and displacement, Appl. Sci., vol. 11, no. 22, pp. 11056, 2021. DOI: 10.3390/app112211056.

[53] J. Liu, M. Mohammadi, Y. Zhan, P. Zheng, M. Rashidi, and P. Mehrabi, Utilizing artificial intelligence to predict the superplasticizer demand of self-consolidating concrete incorporating pumice, slag, and fly ash powders, Materials, vol. 14, no. 22, pp. 6792, 2021. DOI: 10.3390/ma14226792.

[54] E. Taheri, A. Firouzianhaji, P. Mehrabi, B. Vosough Hosseini, and B. Samali, Experimental and numerical investigation of a method for strengthening cold-formed steel profiles in bending, Appl. Sci., vol. 10, no. 11, pp. 3855, 2020. DOI: 10.3390/app10113855.

[55] Y. Feng, M. Mohammadi, L. Wang, M. Rashidi, and P. Mehrabi, Application of artificial intelligence to evaluate the fresh properties of self-consolidating concrete, Materials, vol. 14, no. 17, pp. 4885, 2021. DOI: 10.3390/ma14174885.

[56] A. Firouzianhaji, N. Usefi, B. Samali, and P. Mehrabi, Shake table testing of standard cold-formed steel storage rack, Appl. Sci., vol. 11, no. 4, pp. 1821, 2021. DOI: 10.3390/app11041821.

[57] P. Mehrabi, S. Honarbari, S. Rafiei, S. Jahandari, and M. Alizadeh Bidgoli, Seismic response prediction of FRC rectangular columns using intelligent fuzzy-based hybrid metaheuristic techniques, J. Ambient Intell. Humaniz. Comput., vol. 12, no. 11, pp. 10105–10123, 2021. DOI: 10.1007/s12652-020-02776-4.

[58] A. Toghroli, P. Mehrabi, M. Shariati, N.T. Trung, S. Jahandari, and H. Rasekh, Evaluating the use of recycled concrete aggregate and pozzolanic additives in fiber-reinforced pervious concrete with industrial and recycled fibers, Constr. Build. Mater., vol. 252, pp. 118997, 2020. DOI: 10.1016/j.conbuildmat.2020.118997.

[59] Y. Qiu, and J. Wang, A Machine Learning Approach to Credit Card Customer Segmentation for Economic Stability. In Proceedings of the 4th International Conference on Economic Management and Big Data Applications, ICEMBDA 2023, October 27–29, 2023, Tianjin, China. 2024.

[60] Y. Qiu, Estimation of tail risk measures in finance: Approaches to extreme value mixture modeling. Johns Hopkins University, Diss. Johns Hopkins University, 2019.

[61] N.N. Rogacheva. The Theory of Piezoelectric Shells and Plates, CRC Press, 2020.

[62] E. Carrera, M. Cinefra, M. Petrolo, and E. Zappino. Finite Element Analysis of Structures through Unified Formulation, John Wiley & Sons, 2014.

[63] K. Bathe, and E.N. Dvorkin, A Formulation of general shell elements—the use of mixed interpolation of tensorial components, Numer. Methods Eng., vol. 22, no. 3, pp. 697–722, 1986. DOI: 10.1002/nme.1620220312.

[64] M.L. Bucalem, and K. Bathe, Higher-order MITC general shell elements, Numer. Methods Eng., vol. 36, no. 21, pp. 3729–3754, 1993. DOI: 10.1002/nme.1620362109.

[65] M. Cinefra, and S. Valvano, A variable kinematic doubly-curved MITC9 shell element for the analysis of laminated composites, Mech. Adv. Mater. Struct., vol. 23, no. 11, pp. 1312–1325, 2016. DOI: 10.1080/15376494.2015.1070304.

[66] F. Durbin, Numerical inversion of Laplace Transforms: an efficient improvement to Dubner and Abate's method, Comput. J., vol. 17, no. 4, pp. 371–376, 1974. DOI: 10.1093/comjnl/17.4.371.

[67] P. Mehrabi, M. Shariati, K. Kabirifar, M. Jarrah, H. Rasekh, N.T. Trung, A. Shariati, and S. Jahandari, Effect of pumice

powder and nano-clay on the strength and permeability of fiber-reinforced pervious concrete incorporating recycled concrete aggregate, Constr. Build. Mater., vol. 287, pp. 122652, 2021. DOI: 10.1016/j.conbuildmat.2021.122652.

[68] E. Taheri, A. Firouzianhaji, N. Usefi, P. Mehrabi, H. Ronagh, and B. Samali, Investigation of a method for strengthening perforated cold-formed steel profiles under compression loads, Appl. Sci., vol. 9, no. 23, pp. 5085, 2019. DOI: 10.3390/app9235085.

[69] J.N. Reddy, and Z.-Q. Cheng, Three-dimensional thermomechanical deformations of functionally graded rectangular plates, Eur. J. Mech. A/Solids, vol. 20, no. 5, pp. 841–855, 2001. DOI: 10.1016/S0997-7538(01)01174-3.

[70] Z. Gou, C. Wang, Z. Han, T. Nie, and H. Tian, Artificial neural networks assisting the design of a dual-mode photonic crystal nanobeam cavity for simultaneous sensing of the refractive index and temperature, Appl. Opt., vol. 61, no. 16, pp. 4802–4808, 2022. DOI: 10.1364/AO.453818.